

# Exploiting the Condensation Reactions of Acetophenone to Engineer Carbon-Encapsulated Nb<sub>2</sub>O<sub>5</sub> Nanocrystals for High-Performance Li and Na Energy Storage Systems

Xianying Han, Patrícia A. Russo,\* Nicolas Goubard-Bretesché, Salvatore Patanè, Saveria Santangelo, Rui Zhang, and Nicola Pinna\*

Efficient synthetic methods to produce high-performance electrode-active materials are crucial for developing energy storage devices for large-scale applications, such as hybrid supercapacitors (HSCs). Here, an effective approach to obtain controllable carbon-encapsulated T-Nb<sub>2</sub>O<sub>5</sub> nanocrystals (NCs) is presented, based on the solvothermal treatment of NbCl<sub>5</sub> in acetophenone. Two separate condensation reactions of acetophenone generate an intimate and homogeneous mixture of Nb<sub>2</sub>O<sub>5</sub> particles and 1,3,5-triphenylbenzene (TPB), which acts as a unique carbon precursor. The electrochemical performance of the resulting composites as anode electrode materials can be tuned by varying the Nb<sub>2</sub>O<sub>5</sub>/TPB ratio. Remarkable performances are achieved for Li-ion and Na-ion energy storage systems at high charge–discharge rates (specific capacities of ≈90 mAh g<sup>-1</sup> at 100 C rate for lithium and ≈125 mAh g<sup>-1</sup> at 20 C for sodium). High energy and power densities are also achieved with Li- and Na-ion HSC devices constructed by using the Nb<sub>2</sub>O<sub>5</sub>/C composites as anode and activated carbon (YPF-50) as cathode, demonstrating the excellent electrochemical properties of the materials synthesized with this approach.

## 1. Introduction

Energy storage technologies such as lithium-ion batteries (LIBs) and electrochemical capacitors (ECs) are currently the focus of intense research for applications that include electronic devices and electric vehicles.<sup>[1–3]</sup> Owing to the different energy storage mechanisms, batteries are able to deliver high energy density, while ECs have comparatively lower energy density but higher power density and longer cycling stability.<sup>[4–6]</sup> The expected technological advancements and increase in global energy consumption over the next decades will require energy storage devices with higher power densities, large capacities, and longer lifespans, compared to those currently available.


Nonaqueous hybrid supercapacitors (HSCs), which generally consist of a battery-type anode (e.g., LIB) and an EC cathode in order to combine the advan-

tages of both system storage mechanisms, are promising energy storage systems to meet future energy demands.<sup>[7–9]</sup> HSCs cathode materials are typically high surface area carbons, with the charge stored at the interface between the electrode and liquid electrolyte, and show high power density, high rate capability, and cycling stability.<sup>[10,11]</sup> At the battery-type anode, charges are usually stored through a Li<sup>+</sup> intercalation mechanism.<sup>[12]</sup> Therefore, the rate performance of HSCs is limited by the slow kinetics of lithium diffusion in the solid, as the surface adsorption–desorption processes at the cathode are considerably faster than the Faradaic reactions that take place at the anode.<sup>[13,14]</sup> Several materials, including Nb<sub>2</sub>O<sub>5</sub>,<sup>[15–17]</sup> Li<sub>4</sub>Ti<sub>5</sub>O<sub>12</sub>,<sup>[18]</sup> TiO<sub>2</sub>,<sup>[19]</sup> V<sub>2</sub>O<sub>5</sub>,<sup>[20]</sup> VN,<sup>[21]</sup> and MnO,<sup>[22]</sup> are being investigated as anodes to fabricate HSCs. In particular, Nb<sub>2</sub>O<sub>5</sub> shows promise due to its high theoretical specific capacity (≈200 mAh g<sup>-1</sup>), fast Li ions' diffusion, and good cycling stability.<sup>[23]</sup> Despite the charge storage deriving from the insertion of Li ions into the structure, the electrochemical behavior of Nb<sub>2</sub>O<sub>5</sub> is similar to that of a pseudocapacitive material. This mechanism has been named intercalation pseudocapacitance, and it is characterized by fast Faradaic processes occurring during ion insertion–deinsertion into the host material.<sup>[8]</sup> It has been demonstrated that the performance of Nb<sub>2</sub>O<sub>5</sub> strongly

X. Han, Dr. P. A. Russo, Dr. N. Goubard-Bretesché,  
Dr. R. Zhang, Prof. N. Pinna  
Institut für Chemie and IRIS Adlershof  
Humboldt-Universität zu Berlin  
Brook-Taylor-Str. 2, 12489 Berlin, Germany  
E-mail: patricia.russo@hu-berlin.de; nicola.pinna@hu-berlin.de

Dr. S. Patanè, Prof. S. Santangelo  
Dipartimento di Ingegneria Civile dell'Energia  
dell'Ambiente e dei Materiali (DICEAM)  
Università "Mediterranea,"  
89122 Reggio Calabria, Italy

Dr. S. Patanè  
Dipartimento di Scienze Matematiche e Informatiche  
Scienze Fisiche e Scienze della Terra (MIFT)  
Università di Messina  
98166 Messina, Italy

 The ORCID identification number(s) for the author(s) of this article can be found under <https://doi.org/10.1002/aenm.201902813>.

© 2019 The Authors. Published by WILEY-VCH Verlag GmbH & Co. KGaA, Weinheim. This is an open access article under the terms of the Creative Commons Attribution-NonCommercial-NoDerivs License, which permits use and distribution in any medium, provided the original work is properly cited, the use is non-commercial and no modifications or adaptations are made.

DOI: 10.1002/aenm.201902813

depends on the crystalline structure, with the orthorhombic structure (T-Nb<sub>2</sub>O<sub>5</sub>, where T derives from “Tief,” meaning low in German) offering unique low steric hindrance diffusion pathways for Li ions that lead to fast ion intercalation and deintercalation.<sup>[23,24]</sup> Nevertheless, the performance of Nb<sub>2</sub>O<sub>5</sub> electrodes is still limited by slow ion diffusion into the bulk and by the low electrical conductivity of the oxide.<sup>[7]</sup> Nanostructuring is a strategy commonly used to improve the capacity and rate capability of electrode materials.<sup>[25]</sup> Decreasing the size to the nanoscale leads to short diffusion paths for ions and electron transport, which can lead to increased power and fast charging in batteries.<sup>[26]</sup> Therefore, several types of Nb<sub>2</sub>O<sub>5</sub> nanostructures have been investigated, including nanowires,<sup>[17,27]</sup> nanorod films,<sup>[28]</sup> nanofibers,<sup>[29]</sup> and nanosheets.<sup>[30,31]</sup> Nevertheless, the synthesis of small nanocrystals (NCs) with sizes below 10 nm remains challenging because the orthorhombic phase is obtained by thermal treatment at temperatures above ≈600 °C.<sup>[32]</sup> At these high temperatures, nanoparticles tend to sinter, producing solids with sizes well above 100 nm or even in the micrometer range.<sup>[33]</sup> On the other hand, to counter the low electrical conductivity, niobium pentoxide is often combined with carbon materials to produce conductive composites. Graphene-related materials (e.g., reduced graphene oxide, rGO) are commonly used as support for Nb<sub>2</sub>O<sub>5</sub> particles or films due to their high conductivity and high surface area.<sup>[7,34,35]</sup> The oxide nanostructures can also be coated with amorphous carbon via postsynthesis procedures, although it is difficult to obtain homogeneous coatings of the surface as particles tend to agglomerate.<sup>[36,37]</sup> Nb<sub>2</sub>O<sub>5</sub>/C composites have also been synthesized through thermal treatment of the oxide nanoparticles containing surfactant molecules attached to the surface. However, methods that allow us to simultaneously control the Nb<sub>2</sub>O<sub>5</sub> size, composite morphology, porosity, and carbon content through simple experimental steps are still needed to produce high-performance electrode materials.

Nb<sub>2</sub>O<sub>5</sub> has been mostly investigated as an anode electrode material for lithium-ion batteries and hybrid supercapacitors.<sup>[35,38–41]</sup> The abundance and low cost of sodium compared to lithium have led to a recent increased interest in sodium-ion energy storage devices.<sup>[42–44]</sup> However, the larger size of the sodium ion compared to lithium causes slow diffusion of the Na ions inside the structure of Nb<sub>2</sub>O<sub>5</sub>, which results in low capacities and fast capacity loss with the increase of the current density.<sup>[43]</sup> Therefore, enhancing the Na-ion rate performance of Nb<sub>2</sub>O<sub>5</sub>-based electrodes remains a demanding task.

Here, we present an effective and simple method to fabricate composites consisting of carbon-encapsulated T-Nb<sub>2</sub>O<sub>5</sub> nanocrystals, by exploiting the acid-catalyzed condensation reactions of acetophenone to produce intimate mixtures of Nb<sub>2</sub>O<sub>5</sub> and 1,3,5-triphenylbenzene (TPB). The latter is used as a monomer in the synthesis of porous polymers, which, combined with its aromatic nature, makes it a suitable precursor for porous carbon. This approach allows us to control the morphology of the composites, as well as the particle size and carbon content by varying the Nb<sub>2</sub>O<sub>5</sub>/TPB ratio, and to tune the electrochemical performance. Consequently, excellent high rate performances were achieved for the optimized materials as anodes in energy storage devices based on Li-ion and Na-ion intercalation. Specifically, remarkable capacities of 90 mAh g<sup>-1</sup> at 100 C rate and 125 mAh g<sup>-1</sup> at 20 C

rate were obtained for the Li- and Na-ion energy storage systems, respectively. The excellent electrochemical behavior was further demonstrated by applying the composites as anode electrode materials in Li- and Na-ion hybrid supercapacitors, which were able to deliver high energy and power densities.

## 2. Results and Discussion

Nanostructures consisting of carbon-coated T-Nb<sub>2</sub>O<sub>5</sub> NCs were prepared by a solvothermal reaction in acetophenone, followed by thermal treatment of the resulting inorganic–organic product. **Figure 1** illustrates the preparation procedure and displays the chemical reactions used for synthesizing the materials. First, niobium pentoxide is formed as the side product of the aldol condensation reaction of acetophenone promoted by NbCl<sub>5</sub> (Lewis acid), according to the equation given in Figure 1a (the proposed mechanism is shown in Figure S1 in the Supporting Information). The reaction was confirmed by NMR analysis of the synthesis solution, which revealed the formation of 1,3-diphenyl-2-buten-1-one (Figure S1, Supporting Information). This mechanism is normally involved in the nonaqueous synthesis of metal oxides in ketones.<sup>[45]</sup> Using NbCl<sub>5</sub> as the precursor, it generates small Nb<sub>2</sub>O<sub>5</sub> nanoparticles of low crystallinity (Figures S2 and S3, Supporting Information). The niobium oxide and HCl, produced by the aldol condensation reaction, subsequently catalyze the condensation of the acetophenone into TPB, according to the equation given in Figure 1b (Figure S4, Supporting Information). It is well known that strong acids, such as HCl, catalyze the conversion of acetophenone into TPB.<sup>[46]</sup> However, niobium oxide was also found to be an active catalyst for this conversion. The TPB yield of the reaction of NbCl<sub>5</sub> (0.5 mmol) and acetophenone (20 mL) at 220 °C for 48 h was 16.8% (the yield is defined as the molar ratio  $n_{\text{TPB}}/n_{\text{acetophenone}}/3$ ). The Nb<sub>2</sub>O<sub>5</sub> nanoparticles (NPs) synthesized in this way, after the complete removal of TPB, were heated again in 20 mL of acetophenone at 220 °C for 48 h and led to a TPB yield of 13.4%, demonstrating the catalytic activity of the Nb<sub>2</sub>O<sub>5</sub> NPs for the condensation of acetophenone into TPB. The final solid product after the 48 h reaction of NbCl<sub>5</sub> with acetophenone is an intimate and homogeneous mixture of oxide and TPB (Figures S2 and S4, Supporting Information). It was found that short synthesis times (e.g., <30 min) produce the oxide but not TPB, confirming that the reactions take place consecutively. Thermal treatment of the Nb<sub>2</sub>O<sub>5</sub>/TPB mixtures at 700 °C under argon was applied for carbonizing the organic (Figure S4, Supporting Information), as well as to increase the crystallization degree of the niobium oxide and generate the T-Nb<sub>2</sub>O<sub>5</sub>/C composites. The carbon content of the composites was varied between 0 and 16 wt% by changing the Nb<sub>2</sub>O<sub>5</sub>/TPB ratio, which was achieved by removing the desired amount of TPB with acetone. Two composite morphologies were produced using this approach. Small carbon-encapsulated Nb<sub>2</sub>O<sub>5</sub> NCs (NP-X where X is the carbon content samples) were synthesized by reaction of NbCl<sub>5</sub> with acetophenone (Figure 1c). Spherical structures (400–600 nm) consisting of carbon-coated Nb<sub>2</sub>O<sub>5</sub> NCs (NS-X where X is the carbon content samples) were synthesized by reacting NbCl<sub>5</sub> in acetophenone in the presence of Co<sup>2+</sup> ions (Figure 1d). X-ray photoelectron spectroscopy (XPS) and energy dispersive X-ray spectroscopy (EDX) analyses showed that the cobalt was not incorporated in the

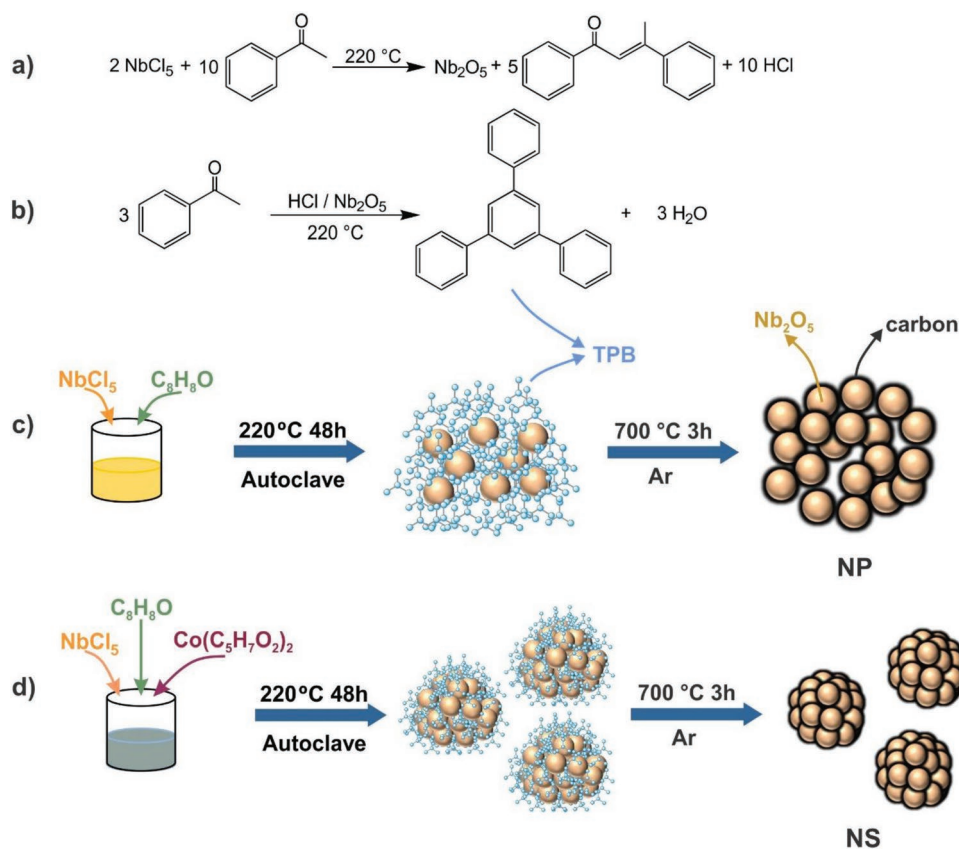


**Figure 1.** a) Reaction of the formation of  $\text{Nb}_2\text{O}_5$  in acetophenone, b) condensation reaction of acetophenone into 1,3,5-triphenylbenzene (TPB), catalyzed by  $\text{Nb}_2\text{O}_5$  and HCl, and schematic representation of the synthesis of the c) NP and d) NS carbon-encapsulated  $\text{Nb}_2\text{O}_5$  composites.

final composites (Figures S5 and S6, Supporting Information), acting only as a promoter of the self-assembly of the particles.<sup>[47]</sup> The carbon wt% in the carbonized samples was determined by thermogravimetric analysis (Figure S7, Supporting Information). NP materials were prepared with 5 wt% carbon (NP-5), 10 wt% carbon (NP-10), and 15 wt% carbon (NP-15), while the spherical assemblies were prepared with 7 wt% carbon (NS-7), 11 wt% carbon (NS-11), and 16 wt% carbon (NS-16). Samples NP-0 and NS-0 are the corresponding materials without carbon.

Figure 2a,b shows the X-ray diffractograms of the NP and NS compounds. All the patterns are assigned to the orthorhombic phase of  $\text{Nb}_2\text{O}_5$  (ICDD file no. 030–0873), and no other phases or impurities are detected. For the pure oxide samples (NP-0 and NS-0), the narrow reflections indicate the presence of large crystallites resulting from the thermal treatment at high temperature. For both types of morphology, the reflections became progressively broader as the carbon content increases, suggesting a decrease of the crystallite size. The results of micro-Raman analysis agree with the indications emerging from the X-ray diffraction (XRD). Figure 2c,d displays the region of the  $\text{Nb}_2\text{O}_5$  phonon modes. Lower-resolution spectra including the region of the  $\text{Csp}^2$  phonon modes ( $>1000 \text{ cm}^{-1}$ ) are shown in Figure S8 (Supporting Information). The spectra of the pure oxide samples are typical of highly crystalline  $\text{Nb}_2\text{O}_5$  with orthorhombic structure.<sup>[48–53]</sup> They are dominated by the intense band (at  $693 \text{ cm}^{-1}$ ) arising from the symmetrical TO

stretch of Nb–O bonds in the low distorted corner- or edge-sharing bipyramidal units of the oxide lattice;<sup>[48,50,52]</sup> weaker bands are further detected at 122, 227, 308, 465, and  $809 \text{ cm}^{-1}$ . The NP and NS composites exhibit similar spectra. This finding confirms the formation of T- $\text{Nb}_2\text{O}_5$  also in the presence of carbon. Nonetheless, all the bands are broader, in agreement with the average crystallite size decrease, evidenced by the broadening of the XRD reflections. The bands originating from the bending of Nb–O–Nb bonds (at 228 and  $308 \text{ cm}^{-1}$ )<sup>[54,55]</sup> are hardly resolved, while the band arising from the vibrations of the octahedra as a whole (at  $122 \text{ cm}^{-1}$ ) is more intense.<sup>[49]</sup> The appearance of a very weak contribution at  $975\text{--}990 \text{ cm}^{-1}$  hints at the presence, in the T- $\text{Nb}_2\text{O}_5$  NCs, of a small content of octahedral distortions due to surface species, such as  $\text{O}=\text{Nb}-\text{O}$ .<sup>[52,53,55]</sup> The strongest band, associated with the bond order of the niobia polyhedra and structure order,<sup>[50,52,53]</sup> undergoes a downshift in all the composites but NP-10, where, on the contrary, it moves toward higher frequencies indicating that more ordered T- $\text{Nb}_2\text{O}_5$  NCs are formed. In fact, NP-10 is the sample with the most ordered niobia NCs.

At higher frequency (Figure S8, Supporting Information), the bands typical of disordered/amorphous nanocarbons<sup>[56]</sup> dominate the spectra, namely the G-band (at  $1598 \text{ cm}^{-1}$ ) and the disorder-activated D-band (at  $1346 \text{ cm}^{-1}$ , for 2.33 eV excitation). The former originates from the  $\text{E}_{2g}$  symmetry stretching of all  $\text{sp}^2$  bonded C=C pairs, whereas the latter is associated with the  $\text{A}_{1g}$  symmetry in-plane breathing mode of the C hexagonal rings.<sup>[56]</sup>

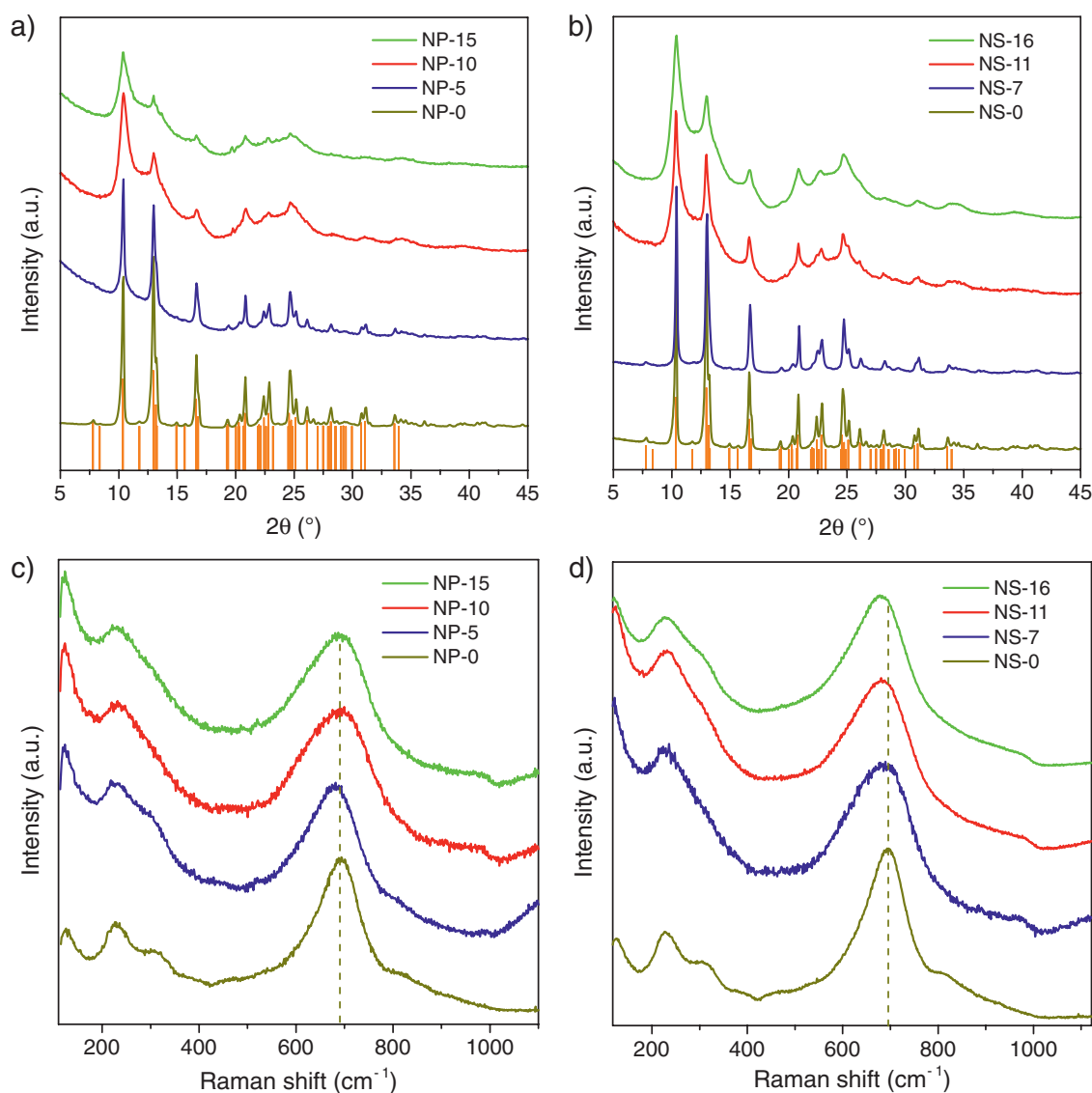


**Figure 2.** X-ray diffraction patterns of the a) NP and b) NS materials prepared using different  $\text{Nb}_2\text{O}_5$ /TPB ratios (vertical bars correspond to the reference pattern of orthorhombic  $\text{Nb}_2\text{O}_5$ - ICDD file no. 030-0873). High-resolution micro-Raman spectra of the c) NP and d) NS materials with various amounts of carbon (spectra are off set and normalized to the maximum intensity of the peak at  $690\text{ cm}^{-1}$  for an easier comparison).

Two weaker bands contribute to the Raman scattering intensity in the first-order region of the spectra (Figure S9a, Supporting Information). The bands centered at  $\approx 1150\text{ cm}^{-1}$  (T-band) and  $1500\text{ cm}^{-1}$  (A-band) reveal the presence of *trans*-polyacetylene-like chains, formed at the zigzag edges of the defective graphitic layers,<sup>[57]</sup> and of amorphous phases, connected to the planes of the aromatic rings through  $\text{Csp}^3$  bonds,<sup>[57,58]</sup> respectively. With increasing carbon content, the relative (to G-band) intensity of the main oxide peak undergoes a slight decrease (Figure S9b, Supporting Information), as expected; on the contrary, the D/G intensity ratio, calculated as peak amplitude ratios, as in the case of large disorder,<sup>[59]</sup> increases (Figure S9c, Supporting Information), suggesting an increased density of  $\text{sp}^2$  defects in the carbonaceous matrix.<sup>[56,59]</sup> The density of non- $\text{sp}^2$  defects, as monitored by the T/G and A/G intensity ratios, increases too (Figure S9c, Supporting Information).

The chemical state of the niobium in the samples was evaluated by XPS. The high-resolution Nb 3d core level of the NP and NS materials (Figure S5, Supporting Information) exhibits the characteristic doublet at binding energies of  $207.4\text{ eV}$  ( $3d_{5/2}$ ) and  $210.2\text{ eV}$  ( $3d_{3/2}$ ), indicating that niobium is present in the materials exclusively with the 5+ oxidation state.<sup>[60]</sup>

Transmission electron microscopy (TEM) and high-resolution TEM (HRTEM) studies were carried out to obtain information on the size, morphology, and crystallinity of the composites (Figure 3; Figure S10, Supporting Information). In the absence of organics, the small NPs synthesized in acetophenone are converted into large crystalline T- $\text{Nb}_2\text{O}_5$  particles upon thermal treatment at  $700\text{ }^\circ\text{C}$  (Figure S10, Supporting Information). The composites NP-10 and NP-15, on the contrary, consist of small  $\text{Nb}_2\text{O}_5$  NCs surrounded by carbon. The HRTEM image (Figure 3c) shows that the oxide NCs have



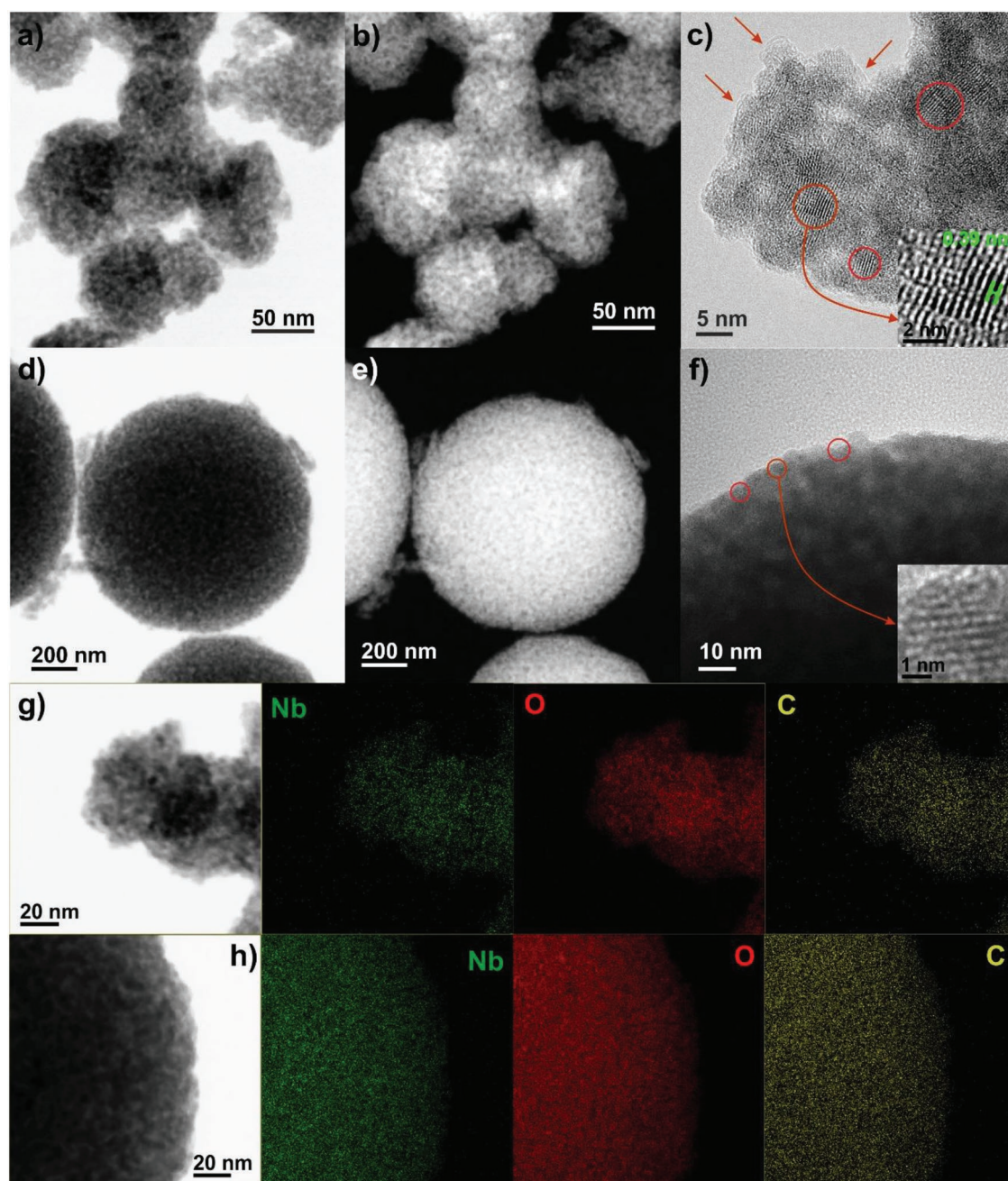


**Figure 3.** a,d) BF-STEM, b,e) STEM-HAADF and c,f) HRTEM images of the carbon-encapsulated  $\text{Nb}_2\text{O}_5$  materials a–c) NP-10 and d–f) NS-16. BF-STEM images of g) NP-10 and h) NS-16 and corresponding EDX elemental mappings of Nb, O, and C.

sizes around 5 nm (indicated by circles) and are coated with carbon (indicated by arrows). The values of the average crystallite sizes estimated from the (001) reflections of the XRD patterns using the Scherrer equation are consistent with the TEM observations (the estimated crystallite sizes are 17.5, 4.5, 4.2, 6.5, 5.7, and 3.8 nm for NP-5, NP-10, NP-15, NS-7, NS-11, and NS-16, respectively). HRTEM further reveals well-defined lattice fringes and the absence of defects on the oxide, indicative of the high crystallinity of the T- $\text{Nb}_2\text{O}_5$  NCs. The distance between the planes of atoms calculated from the HRTEM images is 0.39 nm, which corresponds to the

*d*-spacing of the (001) plane of the orthorhombic  $\text{Nb}_2\text{O}_5$  crystal structure. Spherical structures made of carbon-coated T- $\text{Nb}_2\text{O}_5$  NCs (NS-11 and NS-16) could also be prepared by controlling the amount of organic component on the sample before thermal treatment. The lattice fringes visible on the HRTEM image confirm the high crystallinity of the orthorhombic oxide also in the assemblies (Figure 3f). The composites containing only 5–7 wt% of carbon (NP-5 and NS-7) are heterogeneous in terms of particle size and carbon coating (Figure S10b,f,g, Supporting Information), as confirmed by the larger spatial variations of the relative intensity of the

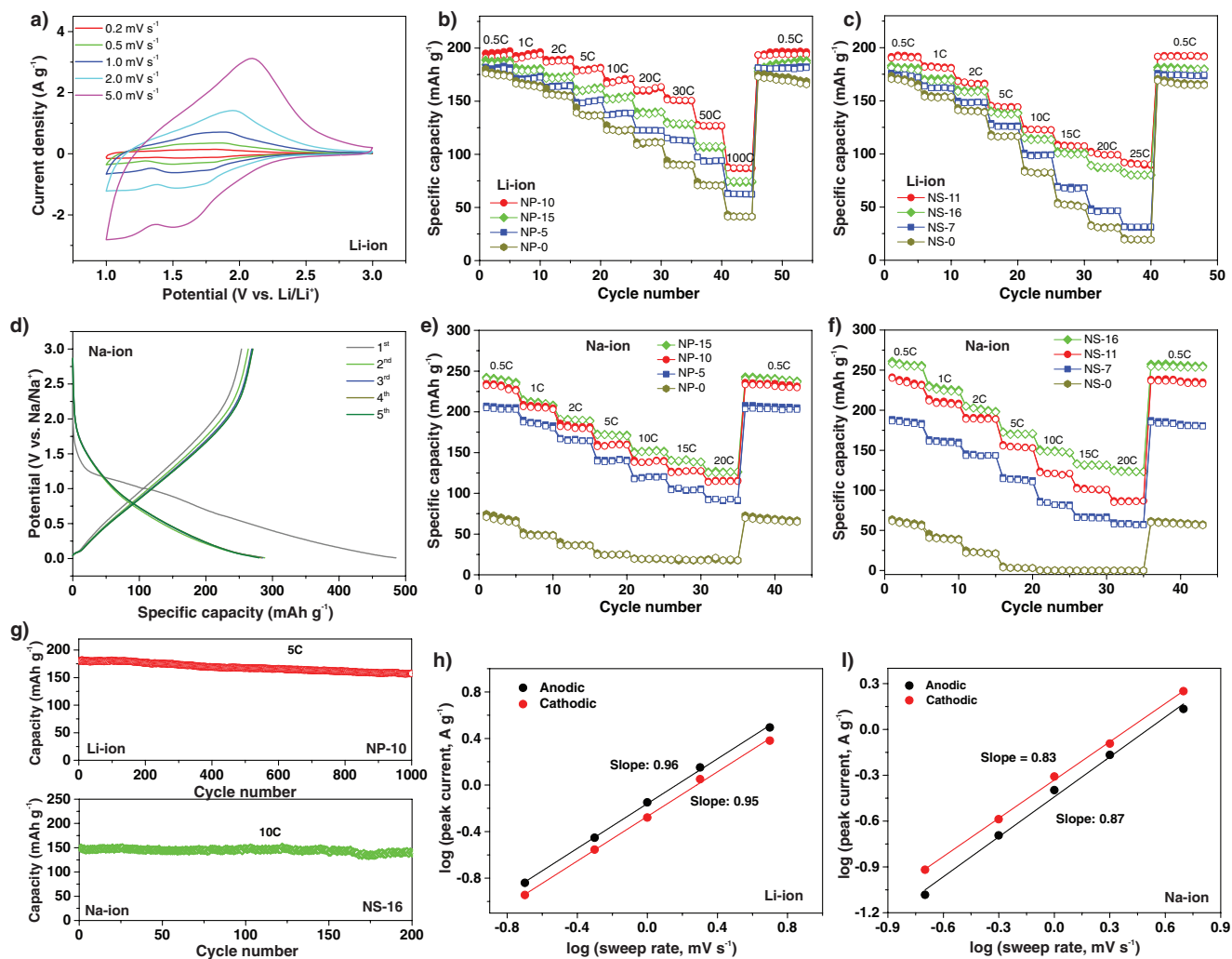


**Figure 4.** Electrochemical performance of the NP and NS materials in the metal-ion half cells. a) CV curves of NP-10, and capacity of the b) NP and c) NS Li-ion half cells at various C rates. d) Galvanostatic charge–discharge curves of NS-16 at 0.25 C, and capacity of the e) NP and f) NS Na-ion half-cells at different C rates. g) Cycling stability of NP-10 at 5 C (Li-ion) and NS-16 at 10 C (Na-ion). Plots of  $\log(i)$  versus  $\log(v)$  for h) NP-10 in the Li-ion half-cell and i) NS-16 in the Na-ion half-cell.

main  $\text{T-Nb}_2\text{O}_5$  band in micro-Raman spectra (Figure S11, Supporting Information). These findings demonstrate the crucial role of TBP in tuning the size of the nanocrystals, by hindering the sintering and growth of the oxide particles at the high temperatures needed to pyrolyze the organic and generate the highly crystalline orthorhombic  $\text{Nb}_2\text{O}_5$  phase. The scanning transmission electron microscopy using a high-angle annular dark-field detector (STEM-HAADF) images of NP-10 and NS-16, in which the brighter regions are associated with the heavier atoms and thick areas while the dark regions correspond to pores, reveal that the composites have porosity (Figure 3; Figure S10, Supporting Information). Figure 3g,h shows STEM-HAADF images of NP-10 and NS-16 and the corresponding EDX mappings for the elements Nb, O, and C in the samples, respectively. The elemental maps show a homogeneous dispersion of the carbon in both the NP and NS samples, suggesting a homogeneous coating of the niobium oxide nanoparticles. The surface textural properties of the composites were evaluated by nitrogen sorption measurements; the

nitrogen sorption isotherms, pore size distributions, and surface areas are shown in Figure S12 and Table S1 (Supporting Information). While NP-0 and NS-0, as expected, have low surface areas of 18 and 29  $\text{m}^2 \text{g}^{-1}$ , respectively, the surface area increases in the composites (e.g., 80 and 100  $\text{m}^2 \text{g}^{-1}$  for NP-10 and NS-16, respectively). In general, the surface areas of the NS composites are higher than those of the NP materials, and a similar trend is observed for the NP and NS samples, with the highest surface area being achieved for the composites with the lowest carbon content (NP-5 and NS-7). The pore size distributions indicate the presence of mesopores in the composites. The composites have mesopores of sizes around 5 nm and, in some cases, also large interparticle mesoporosity. In particular, NP-10 has mainly pores of size below 5 nm whereas NS-16 has pores of sizes around 5 and 25–30 nm. These results indicate that the role of the organic component is threefold: carbon precursor, nanostructuring agent, and porogenic agent.

The electrochemical performance of the NP and NS materials was first investigated for lithium storage. Figure 4a shows

representative cyclic voltammograms (CVs) of the NP-10 electrode at sweep rates ranging from 0.2 to 5 mV s<sup>-1</sup>, in the potential range 1.0–3.0 V (versus Li/Li<sup>+</sup>). The CVs display broad anodic and cathodic peaks, which are attributed to the reversible Li<sup>+</sup> intercalation/deintercalation in the niobium oxide structure, translated by the reaction: Nb<sub>2</sub>O<sub>5</sub> + xLi<sup>+</sup> + xe<sup>-</sup> ↔ Li<sub>x</sub>Nb<sub>2</sub>O<sub>5</sub>. The lithiation of Nb<sub>2</sub>O<sub>5</sub> proceeds up to x = 2, corresponding to a maximum theoretical capacity of ≈200 mAh g<sup>-1</sup>.<sup>[23]</sup>

The electrochemical performance of the Nb<sub>2</sub>O<sub>5</sub>/TPB material (precursor of NP-10) was also evaluated. As shown in Figure S13 (Supporting Information), the Nb<sub>2</sub>O<sub>5</sub>/TPB sample exhibits very poor capacity and rate capability. This result shows that the transformation of the TPB into carbon is essential for achieving the high capacities and rate performances observed for the composites.

Galvanostatic charge–discharge (GCD) measurements were performed to evaluate the rate capability of the NP and NS materials (Figure 4b,c; Figure S14, Supporting Information). For comparison, Figure S15 (Supporting Information) shows also the GCD curves and rate capability of NS-16 in a lithium half-cell, measured in a narrower potential window, which causes a decrease of the capacity at all C rates. Both the NP and NS composites exhibit reversible electrochemical behavior at different current densities, and superior performance compared to the corresponding pure oxides NP-0 and NS-0, especially at high rate (Figure 4b,c; Figure S14, Supporting Information). Electrochemical impedance spectroscopy (EIS) measurements of the half-cells revealed that the charge-transfer resistance is decreased for the composites in comparison with the pure niobium oxide (Figure S16, Supporting Information); moreover, it is affected by the structural disorder of the carbonaceous matrix, as it increases with the D/G intensity ratio (Figure S9c, Supporting Information). The carbon component provides electrical conductivity to the composites, leading to faster electron transport and contributing to their enhanced performance.

The morphology of the samples has a significant effect on the performance, particularly on the rate capability, with the NP composites sustaining higher capacities at high rates compared to the NS materials with similar amounts of carbon. As reported by Kim et al.,<sup>[24]</sup> the Li-ion charge storage in T-Nb<sub>2</sub>O<sub>5</sub> is an intrinsic characteristic of the material, deriving from Faradaic processes and with little influence from the surface area. Therefore, the difference between the behavior of the NP and NS composites can be attributed to the more difficult transport of the Li ions within the spherical assemblies. As a result, the oxide is more readily accessible in the NP nanostructures for fast charge and discharge rates.

As expected, the electrochemical behavior of the composites varies with the carbon amount and T-Nb<sub>2</sub>O<sub>5</sub> particle size. The specific capacities were calculated using the total weight of the composites (i.e., including carbon). For both types of morphologies, the composites made of the smallest oxide particles and 10–11 wt% carbon show higher capacity and rate capability. The samples with 5–7 wt% carbon exhibit significantly worse performance than those with 10–11 wt%, which is attributed to the larger Nb<sub>2</sub>O<sub>5</sub> particles. In fact, the performance of NS-7 can be improved by decreasing the time of the thermal treatment in order to produce smaller Nb<sub>2</sub>O<sub>5</sub> NCs (Figure S17, Supporting Information), thus confirming the important role of the NCs

size on the high rate performance of the composites. The small NCs provide short diffusion paths for Li ions and allow fast intercalation/deintercalation at current densities as high as 20 A g<sup>-1</sup> (100 C rate). The higher amount of carbon on samples NP-15 and NS-16 leads to a slight decrease of the capacity and rate capability compared to NP-10 and NS-11, respectively. The higher amount of carbon surrounding the oxide hinders the accessibility of the lithium ions to the oxide, which, combined with the lower capacity of the amorphous carbon compared with Nb<sub>2</sub>O<sub>5</sub>, causes the slight decrease of the total capacity and rate capability.

To evaluate the role of the carbon source, composites were prepared via postsynthesis coating of the Nb<sub>2</sub>O<sub>5</sub> nanoparticles and spheres synthesized in acetophenone, using glucose as a carbon precursor (experimental details and characterization data are shown in Figures S18 and S19 in the Supporting Information). This is a common method for producing carbon-coated oxide nanomaterials for application as electrode materials. The resulting samples (NP-PS and NS-PS) consist of small sized T-Nb<sub>2</sub>O<sub>5</sub> NCs, and contain ≈20 wt% carbon, which forms dense layers around the oxide (Figures S18 and S19, Supporting Information). These materials show poor electrochemical performance compared with the NP and NS composites (Figure S19, Supporting Information). Therefore, the Nb<sub>2</sub>O<sub>5</sub>/TPB mixture obtained in situ by using acetophenone is crucial for achieving the remarkable performance of the NP and NS composites. This synthesis route leads to an intimate contact between all the particles and carbon, while TPB generates, at the same time, open structures that provide readily access of the Li ions to the oxide. This finding is consistent with the conclusions of a recent study by Sun et al.<sup>[35]</sup>

NS-11 shows the best performance among the NS electrodes, with a capacity of 91 mAh g<sup>-1</sup> at 25 C, which compares favorably with many Nb<sub>2</sub>O<sub>5</sub>-based electrodes described in the literature.<sup>[38,41]</sup> However, NP-10 shows excellent performance at all rates, the best among all the samples investigated. It exhibits a high reversible capacity of ≈192 mAh g<sup>-1</sup> at 0.5 C after the first cycle, which is close to the theoretical capacity, and can still sustain a capacity of 90 mAh g<sup>-1</sup> at the very high current density of 20 A g<sup>-1</sup> (100 C). When the rate is reversed back to 0.5 C, the initial capacity is restored, demonstrating the excellent reversibility of the Li<sup>+</sup> insertion/deinsertion process occurring in the NP-10 electrode. The remarkable high rate behavior of the NP-10 electrode is further confirmed by comparison with the reports in the literature for Nb<sub>2</sub>O<sub>5</sub>-based composites (Table S2, Supporting Information). The performance of NP-10 is comparable to that of a Nb<sub>2</sub>O<sub>5</sub>-holey graphene composite with excellent high rate capability reported by Sun et al.<sup>[35]</sup> The preparation method of NP-10 is, however, simpler and less time consuming. Additionally, NP-10 compares favorably with the other Nb<sub>2</sub>O<sub>5</sub>/C composites described in the literature.<sup>[13,17,38,41,61–63]</sup>

The electrochemical performance of the carbon-encapsulated Nb<sub>2</sub>O<sub>5</sub> samples was further investigated for sodium intercalation (Figure 4d–g). Representative CVs of NP-15 measured in the potential range 0.01–3 V (vs Na/Na<sup>+</sup>) at a sweep rate of 0.1 mV s<sup>-1</sup> (Figure S20, Supporting Information) show an intense cathodic peak between 1.2 and 0.5 V and centered at ≈0.8 V during the first cycle. This feature is consistent with the plateau observed in the galvanostatic curve (Figure 4d) and attributed to the irreversible formation of a solid electrolyte interphase (SEI) at the



electrode–electrolyte interface.<sup>[64,65]</sup> After the first cycle, the CVs show reversible broad cathodic and anodic peaks, as a result of the reaction  $\text{Nb}_2\text{O}_5 + x\text{Na}^+ + xe^- \leftrightarrow \text{Na}_x\text{Nb}_2\text{O}_5$ .

The galvanostatic charge–discharge profiles in Figure 4e,f and Figure S21 (Supporting Information) reveal that, after the first cycle during which the SEI is formed, NP-15 and NS-16 exhibit high reversible capacities ( $\approx 295 \text{ mAh g}^{-1}$  for NS-16, after the first cycle at 0.25 C). In comparison with the study of the materials in a lithium-based electrolyte, the difference between the electrochemical performance of the NP and NS composites and their pure oxide counterparts (NP-0 and NS-0) is even more contrasted. In fact, both NP-0 and NS-0 exhibit poor electrochemical performance, with a low capacity of  $\approx 75 \text{ mAh g}^{-1}$  at 0.5 C that fades rapidly with the increase of the current density. The poorer performances of the NP-0 and NS-0 materials in the sodium systems compared with lithium are consistent with the published data.<sup>[24]</sup> This is attributed to the larger size of the Na ions, which limit their transport within the niobium oxide structure.<sup>[24]</sup> Kim et al.<sup>[66]</sup> have reported that the charge storage in the Na-ion electrolyte involves Na-ion intercalation/deintercalation reactions together with surface capacitive reactions. This is consistent with the stronger effect of the surface area on the sodium storage compared with Li found by Dunn and co-workers.<sup>[24]</sup> In addition, it has been reported that  $\text{Nb}_2\text{O}_5$  undergoes amorphization during the first cycle due to conversion reactions associated with sodium insertion/deinsertion.<sup>[65,66]</sup> This amorphization process was also found to occur with the materials studied here (Figure S22, Supporting Information). Therefore, the combination of low surface area and low electrical conductivity of the pure  $\text{Nb}_2\text{O}_5$  electrodes results in the limited capacity and rate capability. The electrochemical behavior of the composites is significantly enhanced, and the performance improves with the increase of the carbon content of the composites. In particular, NP-15 and NS-16 exhibit high specific capacity and rate capability, with, for example, NS-16 delivering a capacity of  $253 \text{ mAh g}^{-1}$  at 0.5 C and maintaining a high capacity of  $125 \text{ mAh g}^{-1}$  when the rate is increased to 20 C. This can be attributed to the high surface area, small particle size, and conductivity provided by the carbon. The open structures of the composites provide a large surface area and easy access for the sodium electrolyte, and facilitate the electron and Na-ion transport. The performance of the NP-15 and NS-16 materials is superior to that of  $\text{Nb}_2\text{O}_5/\text{C}$  composites described in the literature (for similar mass loadings), demonstrating the promising electrochemical properties of these electrodes (Table S3, Supporting Information).<sup>[42–44,65–68]</sup> For the Na-ion system, the NS morphology does not have a detrimental effect on the performance, as opposed to lithium, which is due to the differences in the charge storage processes occurring in these electrolytes. The higher surface area of the NS material can partly account for this result.

The cycling stability of the materials in the Li and Na electrolytes was also evaluated. Figure 4g shows that NP-10 still retains 88% of its initial capacity after 1000 cycles at 5 C in the Li-ion half-cell, further confirming the high reversibility of the  $\text{Li}^+$  insertion/deinsertion in this sample. NS-16 exhibits a stable capacity of  $\approx 150 \text{ mAh g}^{-1}$  for 200 cycles at 10 C in the Na-ion electrolyte (Figure 4g).

Information about the kinetics of the charge storage in the composites was obtained from the relationship between the

peak current ( $i$ ) of the CVs and the sweep rate ( $v$ ). The relation is expressed by the power law,  $i = av^b$ , where  $a$  and  $b$  are adjustable parameters. The  $b$  parameter, which is determined from the slope of a plot of  $\log(i)$  versus  $\log(v)$ , has a value of 0.5 for a diffusion-controlled process (battery-type kinetics) and a value of 1 for a surface-controlled process (capacitive, fast kinetics).<sup>[23,69,70]</sup> Figure 4h,i shows the plots of  $\log(i)$  versus  $\log(v)$  for the cathodic and anodic peaks of the CVs of NP-10 (Li) and NS-16 (Na). For the NP-10 Li half-cell, the  $b$  value of 0.95–0.96 indicates fast kinetics, demonstrating that the electrochemical behavior of the material is mostly non-diffusion-controlled. This kinetic behavior arises from the low resistance experienced by the lithium ions inside the orthorhombic structure of  $\text{Nb}_2\text{O}_5$ , as demonstrated by Come et al.,<sup>[71]</sup> which, in combination with the small size of the NCs (and thus short diffusion paths), contributes to the excellent high rate capability of NP-10. The lower  $b$ -value obtained for the NS-16 sample in the Na-ion electrolyte indicates a larger contribution of diffusion-controlled processes to the charge storage mechanism, and reflects the slower kinetics of the Na-ion intercalation/deintercalation reactions. The relationship between the peak current of the CVs and the sweep rate can be further applied to evaluate the contributions arising from the capacitive and diffusion-controlled processes to the total capacity of the materials. This relation can be represented by the expression  $i = k_1v + k_2v^{1/2}$ , where  $k_1$  and  $k_2$  are constants,  $k_1v$  represents the capacitive contribution, and  $k_2v^{1/2}$  represents the diffusion-controlled contribution.<sup>[70]</sup> The  $k_1$  and  $k_2$  constants can be evaluated from the plots of  $v^{1/2}$  as a function of  $i/v^{1/2}$ , as described by several authors in the literature.<sup>[23,24,68,70]</sup> For the NP electrodes in the Li half-cells, the capacitive contribution increases with the decrease of the particle size and increase of the carbon content up to 10 wt% and then slightly decreases (Figure S16, Supporting Information). Therefore, NP-10 provides the most suitable structural features for achieving fast Li-ion transport, which leads to the high rate capability of this electrode. The capacitive contribution, associated with fast kinetics, is significantly lower for the Na-ion half-cell than for the Li-ion half-cell (Figure S23, Supporting Information) and a large part of the total capacity derives from diffusion-limited Na intercalation/deintercalation processes due to the larger size of the Na ion. This results in the lower rate capability of the electrode materials in the Na-ion system compared with Li. The surface processes discussed above, which are characterized by fast kinetics, are included in the capacitive contribution. These results are consistent with the performance of the NP and NS materials discussed above.

The electrochemical behavior of selected NP and NS samples was further evaluated by applying the composites as anode electrodes in Li-ion (NP-10) and Na-ion (NP-15, NS-16) hybrid supercapacitors. Commercial activated carbon (AC) was used as the cathode electrode material. The activated carbon stores charge in the electrochemical double layer formed at the interface between the carbon and the electrolyte. This non-Faradaic capacitive storage mechanism is reflected in the rectangular shape of the CVs and linear charge-discharge profiles measured (Figure S24, Supporting Information). A capacitance of  $93 \text{ F g}^{-1}$  (with respect to the mass of the activated carbon) is extracted from the electrochemical measurements at  $40 \text{ mA g}^{-1}$  in a Li-ion cell, which is typical for such a material in an organic electrolyte.



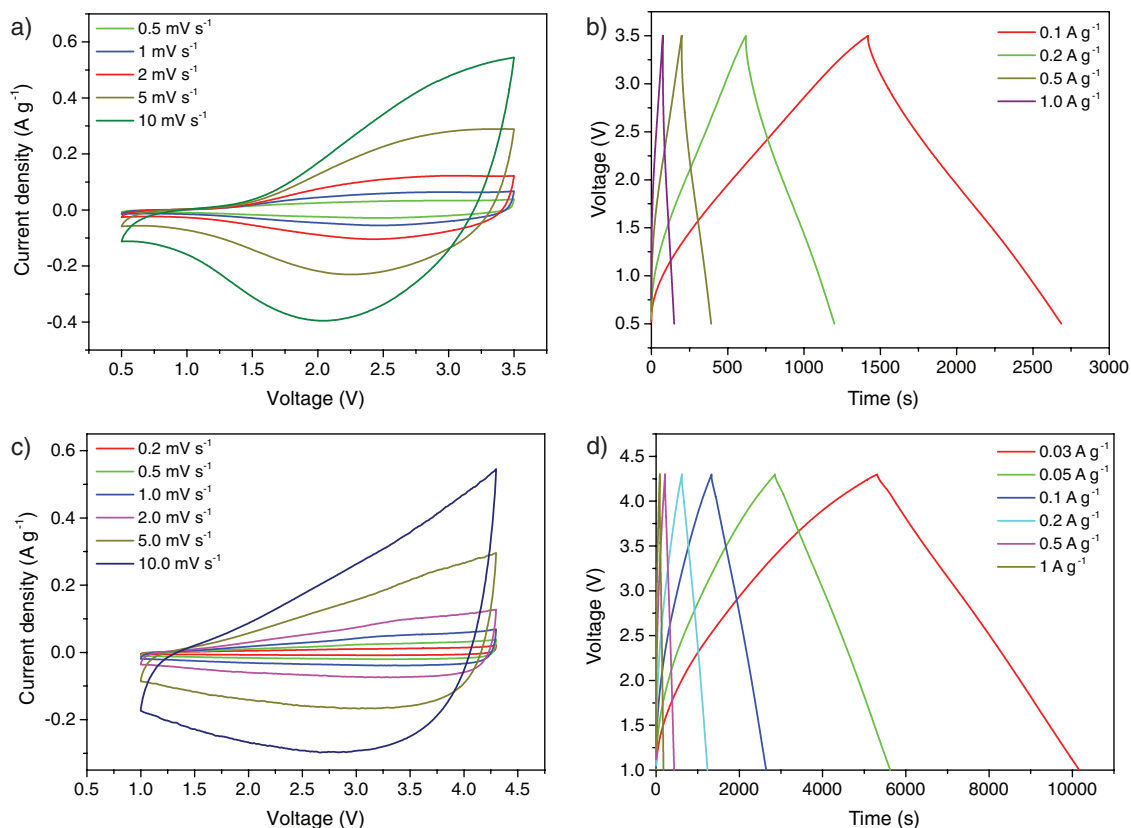


**Figure 5.** Performance of the a,b) Li-ion HSC and c,d) Na-ion HSC devices using NP-10 and NP-15, respectively, as anode electrode materials and commercial activated carbon (YPF-50) at the cathode. a,c) CV curves at different sweep rates. b,d) Galvanostatic charge–discharge profiles at various current densities.

A mass ratio between the composites at the anode and AC at the cathode of 1:3.5 was used for constructing the HSC devices. The shape of the CV curves of the HSCs in the potential ranges of 0.5–3.5 V (Li-ion HSC) and 1.0–4.3 V (Na-ion HSCs) reflects the combination of the Faradaic intercalation processes occurring at the anodes and purely capacitive process based on ion adsorption–desorption taking place at the cathode (Figure 5; Figures S25 and S26, Supporting Information).

The galvanostatic charge–discharge curves were measured at current densities between 0.1 and 1.0 A g<sup>-1</sup> (Li HSC) and between 0.03 and 1 A g<sup>-1</sup> (Na HSC), and have a quasitriangular shape typical of supercapacitors (Figure 5; Figures S25 and S26, Supporting Information). The Li HSC device delivers a maximum energy density ( $E$ ) of 57 Wh kg<sup>-1</sup> (per kg or total mass of active materials) at a power density ( $P$ ) of 75 W kg<sup>-1</sup>, and a maximum  $P$  of 7500 W kg<sup>-1</sup> at an  $E$  of 8.6 Wh kg<sup>-1</sup>. This HSC system exhibits a Coulombic efficiency close to 100% and a capacity retention of 88% over 2000 cycles at a current density of 1 A g<sup>-1</sup> (Figure S27, Supporting Information). The Na-ion HSC devices based on NP-15 and NS-16 also exhibit high power and energy densities (Figure S28, Supporting Information) and fairly stable performance (Figure S27, Supporting Information). The performance of the composite-based HSCs is compared with data from the literature (Figure S28 and Tables S2 and S3, Supporting Information), and demonstrates the promising electrochemical performance of the NP

and NS composites as anode materials for both lithium and sodium HSCs.

### 3. Conclusion

An effective route has been developed to fabricate carbon-encapsulated T-Nb<sub>2</sub>O<sub>5</sub> NCs, based on a simple reaction of a niobium precursor with acetophenone, which generates the oxide nanoparticles and a carbon precursor simultaneously. This is a general method that can be easily extended to produce a variety of metal oxide/carbon composite nanostructures, by exploiting the reactions of ketones. It has been demonstrated that the carbon content and size of the NCs can be controlled, while the addition of assembly promoting agents can be used to further change the morphology of the nanostructures, allowing us to tune the electrochemical properties. The resulting optimized materials exhibited excellent high rate performance as anode electrode materials in Li-ion and Na-ion energy storage devices, sustaining a specific capacity of  $\approx 90$  mAh g<sup>-1</sup> at 100 C rate in a Li-ion electrolyte and  $\approx 125$  mAh g<sup>-1</sup> at 20 C rate in a Na-ion electrolyte. Their excellent electrochemical behavior was further demonstrated as anode-active materials in Li- and Na-ion HSC devices, with activated carbon at the cathode. The unique features of this synthesis route and the materials it produces show great

potential for the development of advanced active electrode materials for energy storage devices.

## 4. Experimental Section

**Synthesis:** To synthesize the Nb<sub>2</sub>O<sub>5</sub> nanoparticles, niobium(V) chloride (0.135 g) was dissolved in 20 mL of acetophenone in a glovebox under argon, and the solution was transferred to a Teflon-lined stainless-steel autoclave, and then heated at 220 °C for 48 h. The product was collected by centrifugation, and washed with ethanol, followed by acetone to dissolve and remove the desired amount of organics (1 mL of acetone dissolves ≈0.1 mmol of the organic TPB; the materials presented here were prepared from Nb<sub>2</sub>O<sub>5</sub>/TPB molar ratios of ≈1:0, 1:1, 1:3, and 1:10). Subsequently, the inorganic–organic mixture was thermally treated under argon flow at 700 °C for 3 h, with a heating rate of 10 °C min<sup>-1</sup>. 3D spherical self-assemblies of nanoparticles with various carbon contents were synthesized in a similar way as described for the nanoparticles, but by additionally adding 0.128 g of cobalt(II) acetylacetonate and stirring the solution for 48 h under argon before transferring to the autoclave. The synthesized samples were denoted NP-*x* (nanoparticles) and NS-*x* (spherical assemblies of NPs), where *x* represents the carbon wt% of the composite determined by thermogravimetric analysis.

**Characterization:** XRD patterns were recorded with a STOE MP diffractometer in transmission configuration using Mo K $\alpha$  radiation ( $\lambda = 0.07093$  nm). TEM and HRTEM images were acquired on a Philips CM 200 and FEI Talos 200S microscope operated at 200 kV. A NT-MDT NTEGRA—Spectra SPM spectrometer, equipped with MS3504i 350 mm monochromator and ANDOR Idus CCD, was utilized to measure Raman scattering, excited by a solid-state laser operating at 2.33 eV (532 nm). The scattered light from the sample was dispersed by an 1800 lines mm<sup>-1</sup> grating and collected by a Mitutoyo high numerical aperture (NA) 100 $\times$  objective (NA = 0.75). In order to obtain a sufficiently high signal-to-noise ratio in the region of the Nb<sub>2</sub>O<sub>5</sub> phonon modes, a laser power of 740  $\mu$ W at the sample surface was utilized. Lower-resolution spectra were further recorded, by the use of a 600 lines mm<sup>-1</sup> grating, to analyze the region of the Csp<sup>2</sup> phonon modes (>1000 cm<sup>-1</sup>). In order to prevent structural damage of the carbon coating induced by local heating, these spectra were recorded by utilizing a very low laser power (110  $\mu$ W at the sample surface). Finally, in order to have a reliable picture of their bulk, spectra from several random positions on each specimen were collected. The spectra were then averaged and quantitatively analyzed. XPS measurements were performed using a Thermo Fischer Scientific ESCALAB 250Xi instrument, with an Al K $\alpha$  source, in constant analyzer energy mode with a pass energy of 50 eV and a spot size of 400  $\mu$ m. A NETZSCH thermoanalyzer STA 409 C Skimmer system, equipped with BALZERS QMG 421, was used to record the thermoanalytical curves. A synthetic air flow of 70 mL min<sup>-1</sup> and a heating rate of 10 °C min<sup>-1</sup> were applied. Nitrogen sorption isotherms at -196 °C were acquired on a Micromeritics ASAP 2020, after degassing the solids at 200 °C overnight.

**Electrochemical Measurements:** The Nb<sub>2</sub>O<sub>5</sub> working electrodes were prepared by homogeneously mixing active materials, carbon black (super C 65) and polyvinylidene fluoride (70:20:10 by weight) in *N*-methyl-2-pyrrolidinone (NMP). Then, the obtained slurries were coated on copper foil and spread with a doctor blade apparatus for a thickness of 250  $\mu$ m (not including the Cu foil), and subsequently dried at 70 °C for 1 h. The dried electrodes were subsequently cold-laminated and punched into 18 mm diameter disks that were dried at 120 °C overnight in a Büchi vacuum oven, before being transferred to an Ar-filled glovebox for coin-cell assembly. The mass loading of all active materials was controlled within the range of 1.1–1.5 mg cm<sup>-2</sup> so that meaningful comparisons between the samples could be made. Both half-cell and full-cell electrochemical measurements were carried out using 2032-type coin cells. Half-cells were assembled using Nb<sub>2</sub>O<sub>5</sub> as the working electrode material and metallic lithium (or sodium) as both counter and reference electrodes. For lithium-based half-cells, 1.0 M LiPF<sub>6</sub> in ethylene carbonate:diethyl carbonate:dimethyl carbonate (EC:DEC:DMC, 1:1:1 vol. ratio) was used as electrolyte, whereas 1 M NaClO<sub>4</sub> solution

in ethylene carbonate:propylene carbonate:fluoroethylene carbonate (EC:PC:FEC, 48:48:4 vol. ratio) was used for Na-ion systems. In both cases, a glass fiber filter (Whatman) served as a separator. The specific capacity values were calculated according to the total mass of the composites, including carbon. Full cells were assembled using Nb<sub>2</sub>O<sub>5</sub>-based electrodes as anodes and AC as a cathode material, in the corresponding Li-ion or Na-ion electrolyte. The AC electrodes were prepared by thoroughly mixing commercial activated carbon (YPF-50, Kuraray), carbon black (Super C65), and polyvinylidene fluoride (80:10:10 by weight) in NMP. The prepared slurries were coated on an aluminum foil. All the subsequent steps were the same as for the Nb<sub>2</sub>O<sub>5</sub>-based electrodes. Prior to assembling the full cells, the niobium oxide electrodes were pre-lithiated or pre-sodiated. The weight ratio of the active materials in the cells was balanced to be 1:3.5 in a voltage window of 0.5–3.5 V for the Li-ion capacitor and 1.0–4.3 V for its sodium counterpart. CV was performed at various scan rates with a Bio-Logic VMP3 potentiostat/galvanostat and the GCD tests were carried out at different C rates, using a LAND electrochemical workstation (Wuhan). In half-cells, the specific capacity values were calculated according to the total mass of the Nb<sub>2</sub>O<sub>5</sub>-based composites, including carbon. In full-cell configuration, the total mass of active materials (in both anode and cathode) was taken into account. The energy and power density values of the full cells were calculated from the GCD results, using the equation  $E = \int_{t_1}^{t_2} V dt = \frac{1}{2} CV$  and  $p = \frac{E}{t}$ , where C is the capacitance based on the total mass of the active materials in both electrodes, V is the working voltage during the discharging process, and t is the discharging time. EIS was performed at open-circuit potential (OCP) in half-cell configuration, by sweeping frequencies from 100 kHz to 10 mHz with an amplitude of 10 mV.

## Supporting Information

Supporting Information is available from the Wiley Online Library or from the author.

## Acknowledgements

X.H. acknowledges the fellowship from the China Scholarship Council (CSC). P.A.R. acknowledges the support from the DFG (RU2012/2-1). S.S. gratefully thanks the Italian Ministry of Education, University and Research (MIUR) for the partial financial support through the PRIN project 2017MCEEY4, TRUST (Towards sustainable, high-performing, all-solid-state sodium-ion batteries). The authors thank C. Erdmann for performing the electron microscopy measurements.

## Conflict of Interest

The authors declare no conflict of interest.

## Keywords

acetophenone, hybrid supercapacitors, Li-ion storage, Na-ion storage, niobium oxide

Received: August 28, 2019

Published online:

[1] W. Li, B. Song, A. Manthiram, *Chem. Soc. Rev.* **2017**, *46*, 3006.

[2] B. C. Melot, J. M. Tarascon, *Acc. Chem. Res.* **2013**, *46*, 1226.

[3] Y. Wang, Y. Song, Y. Xia, *Chem. Soc. Rev.* **2016**, *45*, 5925.

[4] M. Winter, R. J. Brodd, *Chem. Rev.* **2004**, *104*, 4245.

- [5] N.-S. Choi, Z. Chen, S. A. Freunberger, X. Ji, Y.-K. Sun, K. Amine, G. Yushin, L. F. Nazar, J. Cho, P. G. Bruce, *Angew. Chem., Int. Ed.* **2012**, *51*, 9994.
- [6] P. Simon, Y. Gogotsi, *Nat. Mater.* **2008**, *7*, 845.
- [7] X. Wang, G. Li, Z. Chen, V. Augustyn, X. Ma, G. Wang, B. Dunn, Y. Lu, *Adv. Energy Mater.* **2011**, *1*, 1089.
- [8] V. Augustyn, P. Simon, B. Dunn, *Energy Environ. Sci.* **2014**, *7*, 1597.
- [9] A. S. Arico, P. Bruce, B. Scrosati, J.-M. Tarascon, W. Van Schalkwijk, *Nat. Mater.* **2005**, *4*, 366.
- [10] R. Kötz, M. Carlen, *Electrochim. Acta* **2000**, *45*, 2483.
- [11] L. Wei, G. Yushin, *Nano Energy* **2012**, *1*, 552.
- [12] M. Zhi, C. Xiang, J. Li, M. Li, N. Wu, *Nanoscale* **2013**, *5*, 72.
- [13] E. Lim, H. Kim, C. Jo, J. Chun, K. Ku, S. Kim, H. I. Lee, I.-S. Nam, S. Yoon, K. Kang, J. Lee, *ACS Nano* **2014**, *8*, 8968.
- [14] R. Yi, S. Chen, J. Song, M. L. Gordin, A. Manivannan, D. Wang, *Adv. Funct. Mater.* **2014**, *24*, 7433.
- [15] X. Wang, Q. Li, L. Zhang, Z. Hu, L. Yu, T. Jiang, L. Chen, Y. C. Lu, C. Yan, J. Sun, Z. Liu, *Adv. Mater.* **2018**, *30*, 1800963.
- [16] K. Kim, S.-G. Woo, Y. N. Jo, J. Lee, J.-H. Kim, *Electrochim. Acta* **2017**, *240*, 316.
- [17] H. Yang, H. Xu, L. Wang, L. Zhang, Y. Huang, X. Hu, *Chem. - Eur. J.* **2017**, *23*, 4203.
- [18] H.-G. Jung, N. Venugopal, B. Scrosati, Y.-K. Sun, *J. Power Sources* **2013**, *227*, 266.
- [19] Q. Wang, Z. Wen, J. Li, *Adv. Funct. Mater.* **2006**, *16*, 2141.
- [20] Z. Chen, V. Augustyn, X. Jia, Q. Xiao, B. Dunn, Y. Lu, *ACS Nano* **2012**, *6*, 4319.
- [21] R. Wang, J. Lang, P. Zhang, Z. Lin, X. Yan, *Adv. Funct. Mater.* **2015**, *25*, 2270.
- [22] H. Wang, Z. Xu, Z. Li, K. Cui, J. Ding, A. Kohandehghan, X. Tan, B. Zahiri, B. C. Olsen, C. M. B. Holt, D. Mitlin, *Nano Lett.* **2014**, *14*, 1987.
- [23] V. Augustyn, J. Come, M. A. Lowe, J. W. Kim, P.-L. Taberna, S. H. Tolbert, H. D. Abruña, P. Simon, B. Dunn, *Nat. Mater.* **2013**, *12*, 518.
- [24] J. W. Kim, V. Augustyn, B. Dunn, *Adv. Energy Mater.* **2012**, *2*, 141.
- [25] P. Roy, S. K. Srivastava, *J. Mater. Chem. A* **2015**, *3*, 2454.
- [26] S. Goriparti, E. Miele, F. De Angelis, E. Di Fabrizio, R. Proietti Zaccaria, C. Capiglia, *J. Power Sources* **2014**, *257*, 421.
- [27] H. Song, J. Fu, K. Ding, C. Huang, K. Wu, X. Zhang, B. Gao, K. Huo, X. Peng, P. K. Chu, *J. Power Sources* **2016**, *328*, 599.
- [28] B. Deng, T. Lei, W. Zhu, L. Xiao, J. Liu, *Adv. Funct. Mater.* **2018**, *28*, 1704330.
- [29] J. Y. Cheong, J.-W. Jung, D.-Y. Youn, C. Kim, S. Yu, S.-H. Cho, K. R. Yoon, I.-D. Kim, *J. Power Sources* **2017**, *360*, 434.
- [30] M. Liu, C. Yan, Y. Zhang, *Sci. Rep.* **2015**, *5*, 8326.
- [31] H. Li, Y. Zhu, S. Dong, L. Shen, Z. Chen, X. Zhang, G. Yu, *Chem. Mater.* **2016**, *28*, 5753.
- [32] Y. Zhao, X. Zhou, L. Ye, S. Chi Edman Tsang, *Nano Rev.* **2012**, *3*, 17631.
- [33] Z. Z. Fang, H. Wang, *Int. Mater. Rev.* **2008**, *53*, 326.
- [34] H. Yu, L. Xu, H. Wang, H. Jiang, C. Li, *Electrochim. Acta* **2019**, *295*, 829.
- [35] H. Sun, L. Mei, J. Liang, Z. Zhao, C. Lee, H. Fei, M. Ding, J. Lau, M. Li, C. Wang, *Science* **2017**, *356*, 599.
- [36] J. Lin, Y. Yuan, Q. Su, A. Pan, S. Dinesh, C. Peng, G. Cao, S. Liang, *Electrochim. Acta* **2018**, *292*, 63.
- [37] Y.-S. Lin, J.-G. Duh, M.-H. Hung, *J. Phys. Chem. C* **2010**, *114*, 13136.
- [38] M. Y. Song, N. R. Kim, H. J. Yoon, S. Y. Cho, H.-J. Jin, Y. S. Yun, *ACS Appl. Mater. Interfaces* **2017**, *9*, 2267.
- [39] Y. Yoo, Y. C. Kang, *J. Alloys Compd.* **2019**, *776*, 722.
- [40] S. Zhang, J. Wu, J. Wang, W. Qiao, D. Long, L. Ling, *J. Power Sources* **2018**, *396*, 88.
- [41] E. Lim, C. Jo, H. Kim, M.-H. Kim, Y. Mun, J. Chun, Y. Ye, J. Hwang, K.-S. Ha, K. C. Roh, K. Kang, S. Yoon, J. Lee, *ACS Nano* **2015**, *9*, 7497.
- [42] L. Wang, X. Bi, S. Yang, *Adv. Mater.* **2016**, *28*, 7672.
- [43] L. Yang, Y.-E. Zhu, J. Sheng, F. Li, B. Tang, Y. Zhang, Z. Zhou, *Small* **2017**, *13*, 1702588.
- [44] H. Yang, R. Xu, Y. Gong, Y. Yao, L. Gu, Y. Yu, *Nano Energy* **2018**, *48*, 448.
- [45] R. Deshmukh, M. Niederberger, *Chem. - Eur. J.* **2017**, *23*, 8542.
- [46] Y. Zhao, J. Li, C. Li, K. Yin, D. Ye, X. Jia, *Green Chem.* **2010**, *12*, 1370.
- [47] X. Han, S. Wahl, P. A. Russo, N. Pinna, *Nanomaterials* **2018**, *8*, 249.
- [48] D. Chen, J.-H. Wang, T.-F. Chou, B. Zhao, M. A. El-Sayed, M. Liu, *J. Am. Chem. Soc.* **2017**, *139*, 7071.
- [49] L. Kong, C. Zhang, J. Wang, W. Qiao, L. Ling, D. Long, *Sci. Rep.* **2016**, *6*, 21177.
- [50] W. Zhao, W. Zhao, G. Zhu, T. Lin, F. Xu, F. Huang, *Dalton Trans.* **2016**, *45*, 3888.
- [51] M. P. F. Graça, A. Meireles, C. Nico, M. A. Valente, *J. Alloys Compd.* **2013**, *553*, 177.
- [52] R. Brayner, F. Bozon-Verduraz, *Phys. Chem. Chem. Phys.* **2003**, *5*, 1457.
- [53] J. M. Jehng, I. E. Wachs, *Chem. Mater.* **1991**, *3*, 100.
- [54] N. P. de Moraes, R. Bacani, M. L. C. P. da Silva, T. M. B. Campos, G. P. Thim, L. A. Rodrigues, *Ceram. Int.* **2018**, *44*, 6645.
- [55] G. Falk, M. Borlaf, M. J. López-Muñoz, J. C. Fariñas, J. B. Rodrigues Neto, R. Moreno, *J. Mater. Res.* **2017**, *32*, 3271.
- [56] A. C. Ferrari, J. Robertson, *Phys. Rev. B* **2000**, *61*, 14095.
- [57] K. Bogdanov, A. Fedorov, V. Osipov, T. Enoki, K. Takai, T. Hayashi, V. Ermakov, S. Moshkalev, A. Baranov, *Carbon* **2014**, *73*, 78.
- [58] A. Sadezky, H. Muckenhuber, H. Grothe, R. Niessner, U. Pöschl, *Carbon* **2005**, *43*, 1731.
- [59] L. G. Caçado, A. Jorio, E. H. M. Ferreira, F. Stavale, C. A. Achete, R. B. Capaz, M. V. O. Moutinho, A. Lombardo, T. S. Kulmala, A. C. Ferrari, *Nano Lett.* **2011**, *11*, 3190.
- [60] S. Liu, J. Zhou, Z. Cai, G. Fang, Y. Cai, A. Pan, S. Liang, *J. Mater. Chem. A* **2016**, *4*, 17838.
- [61] S. Hemmati, G. Li, X. Wang, Y. Ding, Y. Pei, A. Yu, Z. Chen, *Nano Energy* **2019**, *56*, 118.
- [62] S. Li, T. Wang, W. Zhu, J. Lian, Y. Huang, Y.-Y. Yu, J. Qiu, Y. Zhao, Y.-C. Yong, H. Li, *J. Mater. Chem. A* **2019**, *7*, 693.
- [63] G. Ma, K. Li, Y. Li, B. Gao, T. Ding, Q. Zhong, J. Su, L. Gong, J. Chen, L. Yuan, *ChemElectroChem* **2016**, *3*, 1360.
- [64] J. Ni, W. Wang, C. Wu, H. Liang, J. Maier, Y. Yu, L. Li, *Adv. Mater.* **2017**, *29*, 1605607.
- [65] L. Eunho, J. Changshin, K. M. Su, K. Mok-Hwa, C. Jinyoung, K. Haegyeom, P. Jongnam, R. K. Chul, K. Kisuk, Y. Songhun, L. Jinwoo, *Adv. Funct. Mater.* **2016**, *26*, 3711.
- [66] H. Kim, E. Lim, C. Jo, G. Yoon, J. Hwang, S. Jeong, J. Lee, K. Kang, *Nano Energy* **2015**, *16*, 62.
- [67] Y. Li, H. Wang, L. Wang, Z. Mao, R. Wang, B. He, Y. Gong, X. Hu, *Small* **2019**, *15*, 1804539.
- [68] F. Liu, X. Cheng, R. Xu, Y. Wu, Y. Jiang, Y. Yu, *Adv. Funct. Mater.* **2018**, *28*, 1800394.
- [69] P. Simon, Y. Gogotsi, B. Dunn, *Science* **2014**, *343*, 1210.
- [70] J. Wang, J. Polleux, J. Lim, B. Dunn, *J. Phys. Chem. C* **2007**, *111*, 14925.
- [71] J. Come, V. Augustyn, J. W. Kim, P. Rozier, P.-L. Taberna, P. Gogotsi, J. W. Long, B. Dunn, P. Simon, *J. Electrochem. Soc.* **2014**, *161*, A718.